

Wide-field, high-resolution Fourier ptychographic microscopy

Guoan Zheng^{†*}, Roarke Horstmeyer and Changhuei Yang

We report an imaging method, termed Fourier ptychographic microscopy (FPM), which iteratively stitches together a number of variably illuminated, low-resolution intensity images in Fourier space to produce a wide-field, high-resolution complex sample image. By adopting a wavefront correction strategy, the FPM method can also correct for aberrations and digitally extend a microscope's depth of focus beyond the physical limitations of its optics. As a demonstration, we built a microscope prototype with a resolution of 0.78 μm , a field of view of $\sim 120 \text{ mm}^2$ and a resolution-invariant depth of focus of 0.3 mm (characterized at 632 nm). Gigapixel colour images of histology slides verify successful FPM operation. The reported imaging procedure transforms the general challenge of high-throughput, high-resolution microscopy from one that is coupled to the physical limitations of the system's optics to one that is solvable through computation.

The throughput of an imaging platform is fundamentally limited by the space-bandwidth product (SBP)¹ of its optical system, which is defined as the number of degrees of freedom it can extract from an optical signal. The SBP of a conventional microscope platform is typically in megapixels, regardless of the magnification factor or numerical aperture (NA) used. As a reference point, a standard $\times 20$ microscope objective (MPLN $\times 20$, 0.4 NA, Olympus) has a resolution of 0.8 μm and a 1.1-mm-diameter field of view (FOV), corresponding to an SBP of ~ 7 megapixels. Increasing the SBP of a microscope is fundamentally confounded by the scale-dependent geometric aberrations of its optical elements¹, resulting in a compromise between achievable image resolution and FOV.

In microscopy, however, a large SBP is highly desirable for biomedical applications such as digital pathology, haematology, immunohistochemistry and neuroanatomy. The strong need in biomedicine and neuroscience to digitally image large numbers of histology slides for analysis has prompted the commercial development of sophisticated mechanical scanning microscope systems and lensless microscopy set-ups. Artificially increasing the SBP of an imaging system by mechanical means is suboptimal, as it requires precise control over actuation, optical alignment and motion tracking. Furthermore, a mechanical solution simply accepts the intrinsic resolution limit and SBP of a conventional microscope's optics, neglecting the computationally addressable problem of resolution enhancement. Lensless microscopy methods such as digital in-line holography^{2–4} and contact-imaging microscopy^{5,6} offer unique imaging capabilities, but also present certain drawbacks. For example, digital in-line holography does not work well for contiguous samples, and contact-imaging microscopy requires a sample to be in close proximity to the sensor.

Here, we present a computational imaging method that is capable of providing a scalable SBP for most existing microscopes without involving mechanical scanning or phase measurements. Although the method does require the acquisition of a plurality of images, it does so non-mechanically and accomplishes its SBP improvement using the plural data to overcome the physical limitations of the system's optics.

The imaging method we introduce and demonstrate, termed Fourier ptychographic microscopy (FPM), shares its roots with

interferometric synthetic aperture microscopy^{7–20}, ptychography^{21–27}, phase retrieval^{28–31}, light-field imaging^{32–35}, structured illumination³⁶ and adaptive optics³⁷. It works by iteratively stitching together a number of low-resolution images in Fourier space to recover an accurate high-resolution, high-SBP output image. Unlike systems designed to increase the SBP of a single acquisition³⁸, combining time-sequential measurements for the same goal allows our set-up to maintain a simple and compact form factor. The main design strategy of FPM is similar to that of interferometric synthetic aperture microscopy^{7–20}: expanding the SBP in Fourier space via multi-image fusion. However, because no measured phase information is needed for FPM, our set-up eliminates the design challenges associated with interferometric detection schemes. Furthermore, the image recovery procedure of FPM follows a strategy similar to ptychography (that is, scanning diffraction microscopy)^{21–27}: iteratively solving for a sample estimate that is consistent with many intensity measurements. Unlike ptychography, however, FPM's object support constraints are imposed in the Fourier domain, offering several unique advantages and opportunities.

By adding a simple light-emitting diode (LED) matrix illumination module and applying the FPM reconstruction algorithm, we transform a conventional optical microscope into a high-resolution (0.78 μm , 0.5 NA), wide-FOV ($\sim 120 \text{ mm}^2$) microscope with a final SBP of ~ 1 gigapixel. Our joint optical–digital solution further allows us to exploit adaptive optics-based wavefront correction strategies to compensate for aberrations and expand the depth of focus beyond conventional optical limits. Specifically, we use our FPM procedure to extend a conventional microscope's 80 μm depth of focus to ~ 0.3 mm, creating a platform with a large tolerance to microscope slide placement errors. In the following, we will briefly outline the FPM operation and experimental set-up, discuss how to apply the FPM digital wavefront correction technique, and demonstrate successful gigapixel imaging of a pathology slide.

Principle of FPM

The data collection procedure of FPM is straightforward. A two-dimensional sample is placed at the focal plane of a low-NA microscope objective and a sequence of N images is collected, with the sample successively illuminated by plane waves at N different

Electrical Engineering, California Institute of Technology, Pasadena, California 91125, USA; [†]Present address: Biomedical Engineering and Electrical Engineering, University of Connecticut, Storrs, Connecticut, 06269, USA. *e-mail: gazheng@caltech.edu

angles. As a key distinction from other synthetic aperture techniques, we only acquire intensity images of the sample—no interferometric measurements are needed. The use of a low-NA objective lens allows a large FOV to be captured at the expense of a low spatial resolution. In this section, we assume the sample is located at the in-focus position of the microscope objective. Later, we will demonstrate that computational refocusing of a mispositioned sample is also possible. Based on N collected low-resolution intensity images, we computationally reconstruct a high-resolution image of the sample following the recovery procedure shown in Fig. 1.

Before explaining the procedure, we first note that our recovery process alternates between the spatial (x - y) and Fourier (k_x - k_y) domains, where k represents wavenumber. Second, we assume that illuminating a thin sample by an oblique plane wave with a wavevector (k_x, k_y) is equivalent to shifting the centre of the sample's spectrum by (k_x, k_y) in the Fourier domain. Third, we assume that the filtering function of our objective lens (that is, coherent optical transfer function) in Fourier space is a circular pupil with a radius of $\text{NA} \times k_0$, where $k_0 = 2\pi/\lambda$ is the wavenumber in vacuum.

FPM generates a high-resolution image I_h from a set of N low-resolution measurements, $I_{\text{lm}}(k_x^i, k_y^i)$ (indexed by their illumination wavevector k_x^i, k_y^i , with $i = 1, 2, \dots, N$), as follows. Subscripts h, l and m denote high-resolution, low-resolution and measurement, respectively. The FPM method begins (step 1) by making an initial guess of the high-resolution object function in the spatial domain, $\sqrt{I_h}e^{i\varphi_h}$. A good starting point is to select $\varphi_h = 0$ and I_h as any upsampled low-resolution image (an initial guess with constant value also works). The Fourier transform of the initial guess creates a broad spectrum in the Fourier domain (Fig. 1, left).

Second, we select a small subregion of this spectrum, equivalent to a low-pass filter, and apply Fourier transformation to generate a new low-resolution target image $\sqrt{I_l}e^{i\varphi_l}$ (step 2). The applied low-pass filter shape is a circular pupil, given by the coherent transfer function of the objective lens. The position of the low-pass filter is

selected to correspond to a particular angle of illumination. For example, the subregion enclosed by the red circle in Fig. 1 corresponds to an image collected under normally incident illumination ($k_x^l = 0, k_y^l = 0$).

Third, following the phase retrieval concepts developed by Fienup^{28–31}, we replace the target image's amplitude component $\sqrt{I_l}$ with the square root of the low-resolution measurement obtained under illumination angle i , $\sqrt{I_{\text{lm}}^i}$, to form an updated, low-resolution target image $\sqrt{I_{\text{lm}}^i}e^{i\varphi_l}$. We then apply Fourier transformation to this updated target $\sqrt{I_{\text{lm}}^i}e^{i\varphi_l}$ and replace its corresponding subregion of the high-resolution Fourier space (step 3). In other words, for $i = 1$, we update the area enclosed by the red circle in Fig. 1 with image $I_{\text{lm}}(k_x^1, k_y^1)$ where $k_x^1 = 0, k_y^1 = 0$.

In the fourth step, we repeat steps 2 and 3 (select a small, circular region of k space and update it with measured image data) for other plane wave illuminations. Examples are represented by the green and blue circles in Fig. 1. Each shifted subregion corresponds to a unique, low-resolution intensity measurement $I_{\text{lm}}(k_x^i, k_y^i)$, and each subregion must overlap with neighbouring subregions to assure convergence. This data redundancy requirement is also present in ptychography^{22,39}. This iterative update continues for all N images, at which point the entire high-resolution image in Fourier space has been modified with data from all low-resolution intensity measurements.

Finally, steps 2–4 are repeated until a self-consistent solution is achieved (we typically repeat these steps once or twice, step 5). At the end of this iterative recovery process, the converged solution in Fourier space is transformed to the spatial domain to recover a high-resolution field $\sqrt{I_h}e^{i\varphi_h}$, offering an accurate image of the targeted two-dimensional sample (Fig. 1, right) with a dramatically increased SBP (high-resolution and wide-FOV). A discussion of the computational cost of the above recovery procedure can be found in Supplementary Note S1. We also performed a set of numerical simulations to validate the proposed FPM method (Supplementary Note S2).

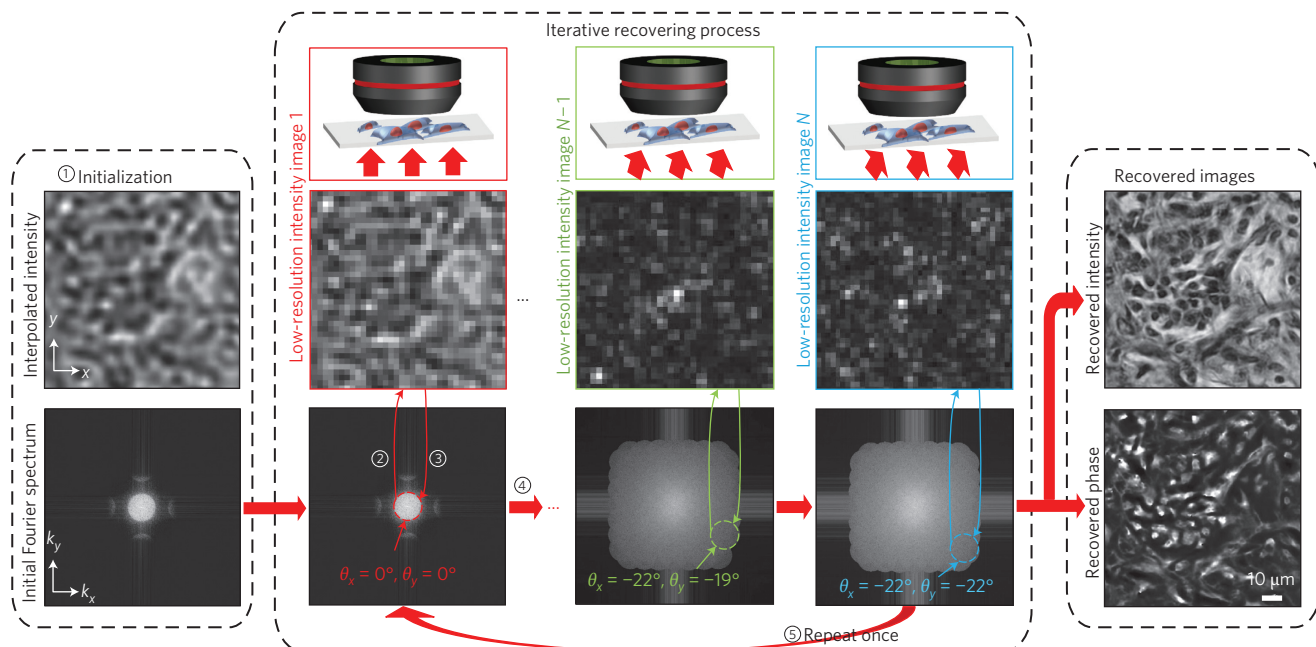


Figure 1 | Iterative recovery procedure of FPM (five steps). N low-resolution intensity images captured under variable illumination are used to recover one high-resolution intensity image and one high-resolution phase map. Steps 1–5 illustrate the FPM algorithm, following principles from phase retrieval. Step 1: initialize the high-resolution image, $\sqrt{I_h}e^{i\varphi_h}$. Step 2: generate a low-resolution image $\sqrt{I_l}e^{i\varphi_l}$, corresponding to an oblique plane-wave incidence. Step 3: replace I_l by the intensity measurement I_{lm} (that is, $\sqrt{I_l}e^{i\varphi_l} \rightarrow \sqrt{I_{\text{lm}}}e^{i\varphi_l}$), and update the corresponding region of $\sqrt{I_h}e^{i\varphi_h}$ in Fourier space (the area within the red circle). Step 4: repeat steps 2–3 for other plane-wave incidences (total of N intensity images). Step 5: repeat steps 2–4 once more.

Drawing connections and distinctions between this iterative process and two related modalities, light-field imaging^{32–35} and ptychography^{21–27}, helps clarify the FPM's principle of operation. A light-field microscope uses a microlens array at its image plane to project M subimages onto its sensor. By extracting different pixels from each subimage, different perspective views can be synthesized, each corresponding to a small aperture of the objective's pupil plane^{32,33}. Similar to a light-field microscope, the FPM set-up also captures multiple perspective images of a sample, corresponding to different, small apertures in the Fourier domain. However, three key differences allow the FPM to create a high-resolution output. First, FPM records larger scattering angles than does a standard light-field microscope. Second, light-field microscopes sacrifice spatial resolution to acquire all perspective images in one single snapshot^{32,33}, whereas FPM acquires each perspective over time. Third, light-field microscopes use the interplay between spatial and angular resolvability to achieve refocusing through a three-dimensional sample, whereas FPM applies this interplay to achieve a different goal: different angular perspectives are synthesized to increase a two-dimensional object's spatial resolution. We also note that an FPM data set of a three-dimensional object can be processed in a similar way as by a light-field microscope to achieve three-dimensional sample refocusing and rendering⁴⁰.

Ptychography^{21–27} is a lensless imaging method that was originally proposed for transmission electron microscopy and brought to fruition by Faulkner and Rodenburg with the introduction of transverse translation diversity^{22,39}. The basic idea of ptychography is to illuminate a sample with a focused beam and repeatedly record its far-field diffraction pattern as a function of sample position. Iterative retrieval methods are then applied to invert the diffraction process and recover the sample's amplitude and phase from this set of measurements. It is clear that FPM and ptychography both iteratively seek a complex field solution that is consistent with many intensity measurements. With ptychography, the object support for phase retrieval is provided by the confined illumination probe in the spatial domain, so the sample (or the probe) must be mechanically scanned through the desired FOV. With FPM, however, the object support is provided by the confined NA in the Fourier domain (a circular pupil). In this regard, FPM appears as the Fourier counterpart of ptychography, justifying the proposed name. By imposing object support in the Fourier domain, FPM naturally offers a large, fixed FOV, a higher signal-to-noise ratio (with focusing elements) and no mechanical scanning, as compared to conventional ptychography. Furthermore, as discussed in the following, FPM can also digitally correct for aberrations common to simple low-NA focusing elements.

Experimental set-up and characterization

To validate the FPM method experimentally, we used an Olympus BX 41 microscope, a $\times 2$ achromatic objective lens (Plan APO, 0.08 NA, Olympus) and an interline charge-coupled device (CCD) camera (Kodak KAI-29050, 5.5- μm pixel size) as our experimental set-up. We then introduced a programmable colour LED matrix placed ~ 8 cm under the sample stage as a variable illumination source (Fig. 2a,b; see Methods). All characterizations were carried out at 632 nm unless otherwise noted.

The resolution improvement provided by the FPM method is demonstrated with a USAF resolution target imaging experiment in Fig. 2c,d (Supplementary Movie S1). Figure 2c1 shows a full-FOV raw intensity image acquired by the FPM platform, and Fig. 2c2 presents a magnified view of the raw data, with a pixel size of 2.75 μm at the object plane (CCD pixel size divided by the magnification factor). The corresponding high-resolution FPM reconstruction is shown in Fig. 2d for comparison, with a maximum synthetic NA of 0.5 set by the maximum angle

between the optical axis and an LED. In our FPM reconstruction, the feature of group 9, element 3 on the USAF target (0.78 μm line width) is clearly resolved. This verifies our prototype platform's expected synthetic NA of 0.5, following the Rayleigh criterion (see Supplementary Fig. S2 for FPM reconstructions with different synthetic NAs and Supplementary Fig. S6 for reconstructed image line traces). In Supplementary Fig. S3, we further determine the depth of focus of the proposed platform to be ~ 100 μm without any computational correction applied, which is approximately equal to the 80 μm depth of focus associated with the $\times 2$ objective used in the experiment, but is ~ 25 -fold longer than that of a conventional microscope objective with a similar 0.5 NA.

Digital wavefront correction

Although the FPM method does not require phase information as an input, its operation implicitly accommodates phase during iterative reconstruction. As we will demonstrate, the depth of focus of our FPM prototype can be significantly extended beyond that of the objective lens using a numerical strategy to compensate for aberrations in the pupil function^{19,41}.

This digital correction process is inspired by similar wavefront correction concepts in adaptive optics³⁷. The basic idea is to digitally introduce a phase map to our coherent optical transfer function to compensate for aberrations at the pupil plane during the iterative image recovery process. The FPM algorithm incorporates this compensation into two additional multiplication steps (steps 2 and 5 in Fig. 3a; Supplementary Fig. S5). Specifically, step 2 models the connection between the actual sample profile and the captured intensity data (with included aberrations) through multiplication with a pupil function $e^{i\varphi(k_x, k_y)}$, whereas step 5 inverts such a connection to achieve an aberration-free reconstructed image. Sample defocus is essentially equivalent to introducing a defocus phase factor to the pupil plane (that is, a defocus aberration):

$$e^{i\varphi(k_x, k_y)} = e^{i\sqrt{(2\pi/\lambda)^2 - k_x^2 - k_y^2}z_0}, k_x^2 + k_y^2 < (\text{NA} \cdot 2\pi/\lambda)^2 \quad (1)$$

where k_x and k_y are the wavenumbers at the pupil plane, z_0 is the defocus distance, and NA is the objective's numerical aperture.

Simulations of the proposed digital wavefront correction strategy are provided in Supplementary Note S2, whereas Fig. 3 experimentally demonstrates FPM's ability to fully resolve an object given a set of intensity images defocused by 150 μm . The significance of wavefront correction is made clear by comparing reconstruction results without (Fig. 3c) or with (Fig. 3d) digital addition of a defocused pupil. We note that, in Fig. 3d, the defocus distance is known *a priori*. If the defocus distance is unknown, we can digitally adjust the 'z' parameter to different values, reconstruct the corresponding FPM images, and pick the sharpest image through observation or by a computer algorithm. This approach can also be extended to image a tilted sample. In this case, we can digitally adjust the 'z' parameter to achieve acuity for each region of the whole image and combine the in-focus regions to form a fully focused image of the tilted sample. From Fig. 3, we conclude that our FPM prototype can achieve a resolution-invariant depth of focus of ~ 0.3 mm with digital wavefront correction (Supplementary Fig. S6). In contrast, the natural depth of focus of our $\times 2$ objective lens (0.08 NA) is ~ 80 μm . The improvement is even more remarkable if compared to an objective lens with a resolution-matching 0.5 NA, where the FPM prototype's 0.3 mm depth of focus offers a ~ 75 factor of improvement.

Finally, we note that alternative digital multiplicative phase factors can be included in steps 2 and 5 to correct for a variety of aberrations, as long as they correctly model the employed optics. In Supplementary Note S4, we provide a simple procedure⁴² for aberration characterizations. Iterative methods in conventional ptychography can also be modified for pupil function recovery in FPM

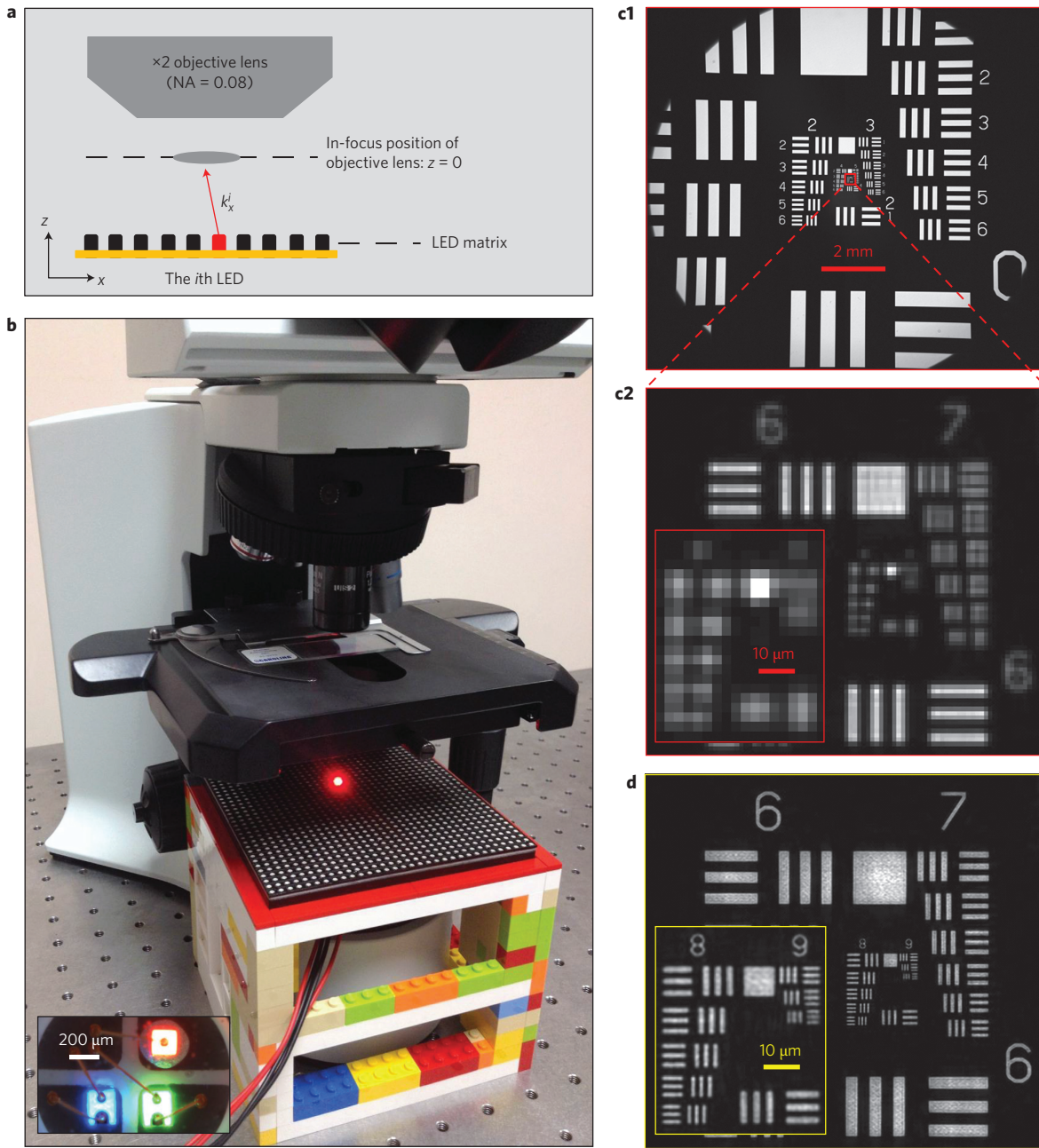


Figure 2 | FPM prototype set-up. **a**, Diagram of set-up. A programmable LED matrix is placed beneath the sample. The i th LED illuminates the sample with wavevector k_x^i . **b**, The LED matrix and microscope used in the experiment, where each LED can provide red, green and blue narrow-band illumination (inset). **c1**, Full-FOV raw image of a USAF resolution target. **c2**, Magnified view of the raw image, with a pixel size of $2.75 \mu\text{m}$. **d**, Our FPM reconstruction of the same region, where we achieve a reconstructed pixel size of $0.275 \mu\text{m}$ (for a discussion of FPM sampling requirement see Supplementary Note 3). In this reconstruction, the corresponding maximum synthetic NA of the reconstructed image is 0.5, set by the maximum angle between the optical axis and an LED. The entire recovery process is demonstrated in Supplementary Movie S1.

settings, and their implementations will be the topic of a future publication. Following the digital wavefront correction strategy, we also correct for the spatially varying aberrations of our prototype's objective lens (see Methods). In Supplementary Fig. S7, we establish that the effective FOV of our prototype is $\sim 120 \text{ mm}^2$.

Gigapixel colour imaging of histology slides

Colour FPM images can be created by simply combining results from red, green and blue LED illumination into each corresponding colour channel. We demonstrate colour FPM with our prototype by acquiring a wide-FOV colour image of a pathology slide (human adenocarcinoma of breast section, Carolina), as shown in Fig. 4.

Vignette high-resolution views are provided in Fig. 4b-d with a reconstructed pixel size of $0.275 \mu\text{m}$. The imaging FOV is $\sim 120 \text{ mm}^2$, the same as that from a $\times 2$ objective (Plan APO, 0.08 NA, Olympus), whereas the maximum achieved NA is 0.5, similar to that of a typical $\times 20$ objective (MPLN, 0.4 NA, Olympus). The conventional microscope images taken with $\times 20$ and $\times 2$ lenses are shown for comparison in Fig. 4c2,c3. In Supplementary Fig. S8, we include a detailed comparison between raw data, FPM reconstruction and a conventional microscope image for two samples: a pathology slide and a blood smear.

The demonstrated SBP of our FPM prototype is ~ 0.9 gigapixels (120 mm^2 FOV divided by $0.37^2 \mu\text{m}^2$ Nyquist pixel area,

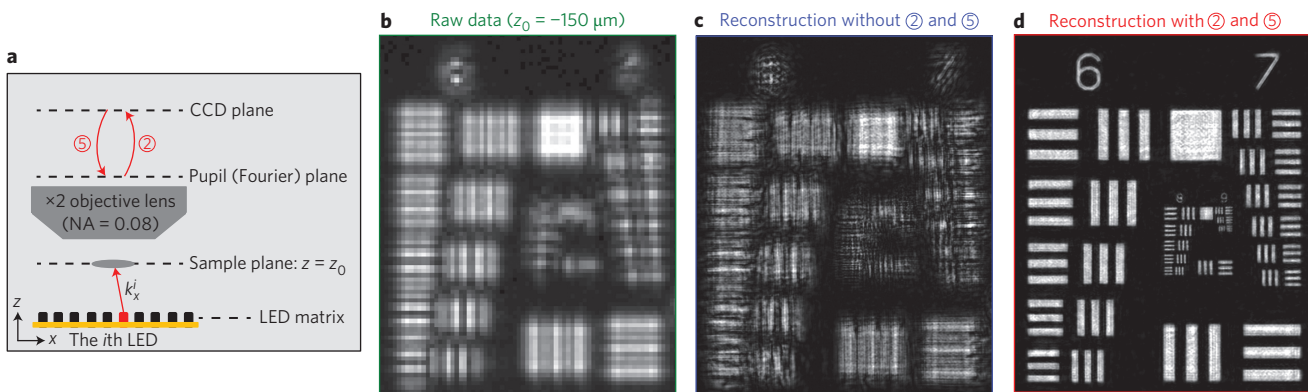


Figure 3 | Extending the depth of focus with digital wavefront correction. **a**, Principle of the FPM digital wavefront correction technique. A digital pupil function is introduced in steps 2 and 5 to model the connection between the actual sample profile and the captured intensity data, which may exhibit aberrations caused by defocus. Step 2: multiply a phase factor $e^{i\varphi(k_x, k_y)}$ in the Fourier domain. Step 5: multiply an inverse phase factor $e^{-i\varphi(k_x, k_y)}$ in the Fourier domain (see Supplementary Fig. S5 for the FPM flowchart with digital wavefront correction). **b**, One raw low-resolution image of the USAF target placed at $z_0 = -150 \mu\text{m}$. **c,d**, High-resolution FPM reconstructions without (**c**) and with (**d**) steps 2 and 5 added to the iterative recovery procedure.

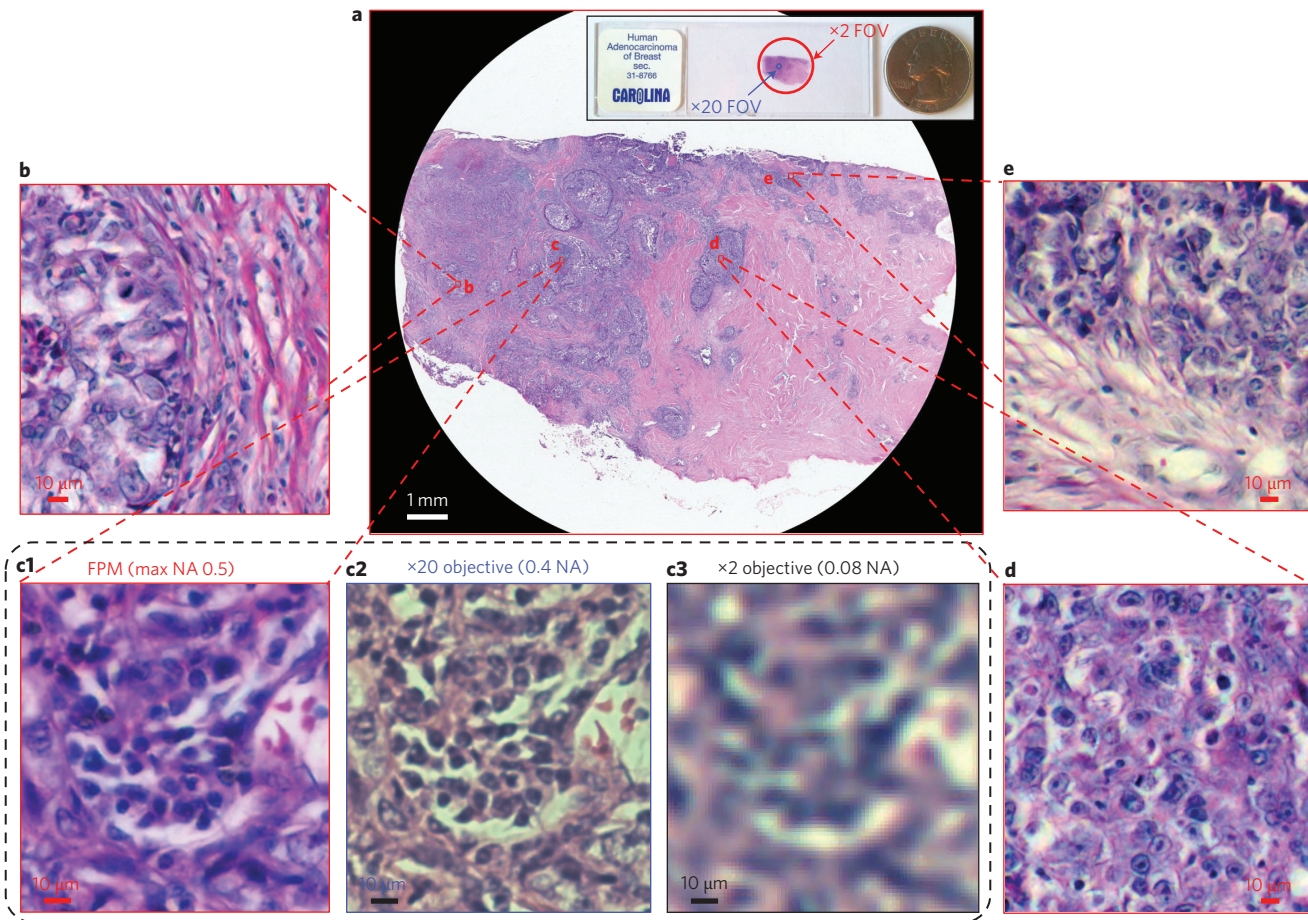


Figure 4 | Gigapixel colour imaging via FPM. **a**, Wide-FOV colour image of a pathology slide, with an SBP of ~ 0.9 gigapixels. **b,c1,d,e**, Vignette high-resolution views of the image in **a**. **c2,c3**, Images taken by a conventional microscope with a $\times 20$ (**c2**) and a $\times 2$ (**c3**) objective lens, for comparison. A colour image sensor (DFK 61BUC02, Image Source) is used for capturing in **c2** and **c3**.

characterized at 632 nm wavelength; Supplementary Note S3). Such a SBP is orders of magnitude larger than that of its constituent $\times 2$ objective (16 megapixels) and that of a typical $\times 20$ objective (7 megapixels). From another perspective, our FPM prototype can be considered a microscope that combines the FOV advantage of a $\times 2$ objective with the resolution advantage of a $\times 20$ objective.

Discussion

We have demonstrated a simple and cost-effective microscopy imaging method, termed Fourier ptychographic microscopy (FPM). This computation-based method is capable of providing a scalable SBP for most conventional microscopes without requiring mechanical scanning. Fundamentally, it transforms the general

challenge of high-throughput microscopy from one that is coupled to the physical limitations of optics to one that is solvable through computation. FPM can be applied to most standard digital microscopes by retrofitting with a readily available LED matrix. Our discussion has focused on generating a high-SBP intensity image. The capability of FPM-enabled phase imaging will be detailed in future work.

Our FPM prototype has not been optimized for performance speed. At present, our imaging speed is limited by the low illumination intensities provided by the LEDs located at the edges of the array. This issue can be addressed by either angling these LEDs inwards or by using higher-power LEDs. Furthermore, the processing speed can be significantly improved by using a graphics processing unit (GPU), as the described algorithm is highly parallelizable. The FPM method requires an overlap of the Fourier-domain spectrum encompassed by each raw image ($\sim 65\%$ spectrum overlap is used in our implementation). This redundancy is necessary as it promotes fast image convergence. It would be worth exploring the exact relationship between data redundancy and convergence speed in the future. In the current FPM method, we also assume that samples are effectively two-dimensional. We believe there are FPM variants that can be developed to handle extended samples. We would also like to reiterate that the current FPM method is not a fluorescence technique, as fluorescent emission profiles would remain unchanged under angle-varied illumination. However, we believe that it is possible to use patterned illumination^{43,44} with FPM variants to increase the SBP of a fluorescence image. Finally, we believe that a more accurate characterization of the back-aperture would be worth implementing in future systems to improve the image quality of the FPM reconstructions.

The ability of FPM to significantly increase the SBP of a conventional microscope is highly useful for addressing the wide-FOV imaging needs that dominate digital pathology and neuroscience. Furthermore, FPM's digital wavefront correction procedure lends extra flexibility to many biomedicine experiments, by largely eliminating the need to maintain a precise working distance between the sample slide and the microscope objective.

However, we believe that FPM is potentially even more broadly transformative. Conventionally, the quality of an imaging system is largely defined by the physical limitations of its optical elements. For example, spatial resolution is generally characterized by the sharpness of the optical system's point-spread function. The proposed FPM method reduces the optical system to a filtering transfer function of the complex field used in an iterative recovery process, through which the characteristics of this complex optical transfer function are rendered nominally irrelevant. As long as the low-pass pupil function is accurately characterized, this link between the actual sample profile and captured data may iteratively improve image resolution. It is this underlying robustness that allows our FPM prototype to render high-resolution images with a low-NA objective that is conventionally incapable of optically providing such a narrow point-spread function and long depth of focus.

More broadly speaking, FPM can be potentially applied to systems with severe but known aberrations to render high-quality images. Our demonstration of digital wavefront correction provides a viable strategy in this respect. We believe that the development of a general aberration correction procedure using our iterative complex field recovery strategy would be very interesting and useful. Furthermore, it has the potential to significantly improve electron, X-ray and terahertz imaging set-ups, which are generally limited by poor and aberrative focusing elements.

Methods

Experimental set-up. The measured distance between the sample stage and the LED array was ~ 8 cm, and the measured working distance of the objective lens was ~ 6 mm. The LED matrix contained 32×32 surface-mounted, full-colour LEDs

(SMD 3528), and the lateral distance between two adjacent LEDs was 4 mm. The central wavelengths of the full-colour LED were 632 nm (red), 532 nm (green) and 472 nm (blue), each offering an approximately spatially coherent quasi-monochromatic source with ~ 20 nm bandwidth.

We used an Atmel ATMEGA-328 microcontroller to provide the logical control for the LED matrix. To achieve maximum brightness, the matrix was driven statically rather than in normal scanning mode, eliminating the duty cycle and boosting currents through the LEDs to a maximum level. The measured light intensities were 0.7, 1.0 and 0.4 W m^{-2} for the red, green and blue colours, respectively. The measured intensities of different individual LEDs were also used to normalize each corresponding intensity image.

Image acquisition and reconstruction. In all figures shown, variable pixel gain was removed by flat-field correction, and hot pixels were identified and removed by interpolation. The sampling requirement of the raw images was $\lambda/(2NA_{\text{obj}})$, where NA_{obj} denotes the NA of the objective lens used (Supplementary Note S3). To reconstruct a high-resolution image with a maximum synthetic NA of 0.5, we used 137 LEDs for illumination (each LED corresponding to a circle in Supplementary Fig. S2c2). Because of the low light intensities of the LEDs, a long exposure time was required by our prototype, limiting the speed of image acquisition. For the central 49 (7×7) LEDs, we acquired three images with three different exposure times (0.005 s, 0.1 s and 0.5 s), and combined them to obtain a 14-bit high-dynamic range (HDR) image for FPM reconstruction. For LEDs outside this central area, we acquired two images with two different exposure times (0.1 s and 0.8 s) to create an 11-bit HDR image. The HDR combination process was used to suppress the saturation error caused by overexposed pixels⁴⁵. The total acquisition time for the current prototype was ~ 3 min. With a brighter LED matrix, the maximum throughput will ultimately be determined by the sensor's data transfer rate. For example, using a commercially available 53 fps (frames per second) full-frame camera (VC-25MX, Vieworks), an acquisition time of several seconds can be achieved for a gigapixel image.

During the reconstruction process, we divided each full FOV raw image ($5,280 \times 4,380$ pixels) into smaller image segments (150×150 pixels each). Each set of image segments was then independently processed by the FPM recovery procedure to create a high-resolution image segment ($1,500 \times 1,500$ pixels). Finally, all high-resolution image segments were combined into one full FOV, high-resolution image (Supplementary Fig. S9). The benefits of dividing the raw image into smaller segments include the following. (1) Each segment of the raw image can be processed independently, a requirement for parallel computing. (2) Memory requirements for computation are reduced. (3) The light from each LED can be accurately treated as a plane wave for each image segment of the raw image. The incident wavevector for each segment can be expressed as

$$(k_x^i, k_y^i) = \frac{2\pi}{\lambda} \left(\frac{(x_c - x_i)}{\sqrt{(x_c - x_i)^2 + (y_c - y_i)^2 + h^2}}, \frac{(y_c - y_i)}{\sqrt{(y_c - y_i)^2 + (y_c - y_i)^2 + h^2}} \right)$$

where (x_c, y_c) is the central position of each small segment of the raw image, (x_i, y_i) is the position of the i th LED, and h is the distance between the LED matrix and the sample. (4) Each small portion can be assigned a specific aberration-correcting pupil function, a common strategy used in wide-field imaging⁴⁶.

Using a personal computer with an Intel i7 CPU (no GPU), the processing time for each high-resolution image segment (converting 150×150 raw pixels to $1,500 \times 1,500$ pixels) was ~ 1.5 s in Matlab. The total processing time for creating a final full FOV image was ~ 10 min. For colour imaging via FPM, we acquired the red, green and blue channels using their corresponding colour LEDs, processing each channel independently. Thus, the total acquisition and processing time for a colour image must be multiplied by a factor of 3.

Received 27 January 2013; accepted 21 June 2013;
published online 28 July 2013

References

1. Lohmann, A. W., Dorsch, R. G., Mendlovic, D., Zalevsky, Z. & Ferreira, C. Space-bandwidth product of optical signals and systems. *J. Opt. Soc. Am. A* **13**, 470–473 (1996).
2. Denis, L., Lorenz, D., Thiébaut, E., Fournier, C. & Trede, D. Inline hologram reconstruction with sparsity constraints. *Opt. Lett.* **34**, 3475–3477 (2009).
3. Xu, W., Jericho, M., Meinertzhagen, I. & Kreuzer, H. Digital in-line holography for biological applications. *Proc. Natl Acad. Sci. USA* **98**, 11301–11305 (2001).
4. Greenbaum, A. *et al.* Increased space-bandwidth product in pixel super-resolved lensfree on-chip microscopy. *Sci. Rep.* **3**, 1717 (2013).
5. Zheng, G., Lee, S. A., Antebi, Y., Elowitz, M. B. & Yang, C. The ePetri dish, an on-chip cell imaging platform based on subpixel perspective sweeping microscopy (SPSM). *Proc. Natl Acad. Sci. USA* **108**, 16889–16894 (2011).
6. Zheng, G., Lee, S. A., Yang, S. & Yang, C. Sub-pixel resolving optofluidic microscope for on-chip cell imaging. *Lab Chip* **10**, 3125–3129 (2010).
7. Turpin, T., Gesell, L., Lapides, J. & Price, C. Theory of the synthetic aperture microscope. *Proc. SPIE* **2566**, 230–240 (1995).

8. Di, J. *et al.* High resolution digital holographic microscopy with a wide field of view based on a synthetic aperture technique and use of linear CCD scanning. *Appl. Opt.* **47**, 5654–5659 (2008).
9. Hillman, T. R., Gutzler, T., Alexandrov, S. A. & Sampson, D. D. High-resolution, wide-field object reconstruction with synthetic aperture Fourier holographic optical microscopy. *Opt. Express* **17**, 7873–7892 (2009).
10. Granero, L., Mico, V., Zalevsky, Z. & Garcia, J. Synthetic aperture superresolved microscopy in digital lensless Fourier holography by time and angular multiplexing of the object information. *Appl. Opt.* **49**, 845–857 (2010).
11. Kim, M. *et al.* High-speed synthetic aperture microscopy for live cell imaging. *Opt. Lett.* **36**, 148–150 (2011).
12. Schwarz, C. J., Kuznetsova, Y. & Brueck, S. Imaging interferometric microscopy. *Opt. Lett.* **28**, 1424–1426 (2003).
13. Feng, P., Wen, X. & Lu, R. Long-working-distance synthetic aperture Fresnel off-axis digital holography. *Opt. Express* **17**, 5473–5480 (2009).
14. Mico, V., Zalevsky, Z., Garcia-Martinez, P. & Garcia, J. Synthetic aperture superresolution with multiple off-axis holograms. *J. Opt. Soc. Am. A* **23**, 3162–3170 (2006).
15. Yuan, C., Zhai, H. & Liu, H. Angular multiplexing in pulsed digital holography for aperture synthesis. *Opt. Lett.* **33**, 2356–2358 (2008).
16. Mico, V., Zalevsky, Z. & Garcia, J. Synthetic aperture microscopy using off-axis illumination and polarization coding. *Opt. Commun.* **276**, 209–217 (2007).
17. Alexandrov, S. & Sampson, D. Spatial information transmission beyond a system's diffraction limit using optical spectral encoding of the spatial frequency. *J. Opt.* **10**, 025304 (2008).
18. Tippie, A. E., Kumar, A. & Fienup, J. R. High-resolution synthetic-aperture digital holography with digital phase and pupil correction. *Opt. Express* **19**, 12027–12038 (2011).
19. Gutzler, T., Hillman, T. R., Alexandrov, S. A. & Sampson, D. D. Coherent aperture-synthesis, wide-field, high-resolution holographic microscopy of biological tissue. *Opt. Lett.* **35**, 1136–1138 (2010).
20. Alexandrov, S. A., Hillman, T. R., Gutzler, T. & Sampson, D. D. Synthetic aperture Fourier holographic optical microscopy. *Phys. Rev. Lett.* **97**, 168102 (2006).
21. Rodenburg, J. M. & Bates, R. H. T. The theory of super-resolution electron microscopy via Wigner-distribution deconvolution. *Phil. Trans. R. Soc. Lond. A* **339**, 521–553 (1992).
22. Faulkner, H. M. L. & Rodenburg, J. M. Movable aperture lensless transmission microscopy: a novel phase retrieval algorithm. *Phys. Rev. Lett.* **93**, 023903 (2004).
23. Rodenburg, J. M. *et al.* Hard-X-ray lensless imaging of extended objects. *Phys. Rev. Lett.* **98**, 034801 (2007).
24. Thibault, P. *et al.* High-resolution scanning X-ray diffraction microscopy. *Science* **321**, 379–382 (2008).
25. Dierolf, M. *et al.* Ptychographic coherent diffractive imaging of weakly scattering specimens. *New J. Phys.* **12**, 035017 (2010).
26. Maiden, A. M., Rodenburg, J. M. & Humphry, M. J. Optical ptychography: a practical implementation with useful resolution. *Opt. Lett.* **35**, 2585–2587 (2010).
27. Humphry, M., Kraus, B., Hurst, A., Maiden, A. & Rodenburg, J. Ptychographic electron microscopy using high-angle dark-field scattering for sub-nanometre resolution imaging. *Nat. Commun.* **3**, 730 (2012).
28. Fienup, J. R. Phase retrieval algorithms: a comparison. *Appl. Opt.* **21**, 2758–2769 (1982).
29. Fienup, J. R. Reconstruction of a complex-valued object from the modulus of its Fourier transform using a support constraint. *J. Opt. Soc. Am. A* **4**, 118–123 (1987).
30. Fienup, J. R. Reconstruction of an object from the modulus of its Fourier transform. *Opt. Lett.* **3**, 27–29 (1978).
31. Fienup, J. R. Lensless coherent imaging by phase retrieval with an illumination pattern constraint. *Opt. Express* **14**, 498–508 (2006).
32. Levoy, M., Ng, R., Adams, A., Footer, M. & Horowitz, M. Light field microscopy. *ACM Trans. Graphics* **25**, 924–934 (2006).
33. Levoy, M., Zhang, Z. & McDowall, I. Recording and controlling the 4D light field in a microscope using microlens arrays. *J. Microsc.* **235**, 144–162 (2009).
34. Arimoto, H. & Javidi, B. Integral three-dimensional imaging with digital reconstruction. *Opt. Lett.* **26**, 157–159 (2001).
35. Hong, S.-H., Jang, J.-S. & Javidi, B. Three-dimensional volumetric object reconstruction using computational integral imaging. *Opt. Express* **12**, 483–491 (2004).
36. Gustafsson, M. G. Surpassing the lateral resolution limit by a factor of two using structured illumination microscopy. *J. Microsc.* **198**, 82–87 (2000).
37. Tyson, R. *Principles of Adaptive Optics* (CRC Press, 2010).
38. Brady, D. *et al.* Multiscale gigapixel photography. *Nature* **486**, 386–389 (2012).
39. Guizar-Sicairos, M. & Fienup, J. R. Phase retrieval with transverse translation diversity: a nonlinear optimization approach. *Opt. Express* **16**, 7264–7278 (2008).
40. Zheng, G., Kolner, C. & Yang, C. Microscopy refocusing and dark-field imaging by using a simple LED array. *Opt. Lett.* **36**, 3987–3989 (2011).
41. Colomb, T. *et al.* Automatic procedure for aberration compensation in digital holographic microscopy and applications to specimen shape compensation. *Appl. Opt.* **45**, 851–863 (2006).
42. Zheng, G., Ou, X., Horstmeyer, R. & Yang, C. Characterization of spatially varying aberrations for wide field-of-view microscopy. *Opt. Express* **21**, 15131–15143 (2013).
43. Wu, J. *et al.* Wide field-of-view microscope based on holographic focus grid illumination. *Opt. Lett.* **35**, 2188–2190 (2010).
44. Wu, J., Zheng, G., Li, Z. & Yang, C. Focal plane tuning in wide-field-of-view microscope with Talbot pattern illumination. *Opt. Lett.* **36**, 2179–2181 (2011).
45. Reinhard, E. *et al.* *High Dynamic Range Imaging: Acquisition, Display, and Image-based Lighting* (Morgan Kaufmann, 2010).
46. Gunturk, B. K. & Li, X. *Image Restoration: Fundamentals and Advances* Vol. 7 (CRC Press, 2012).

Acknowledgements

The authors thank Xiaoze Ou for discussions and help with experiments. The authors acknowledge funding support from the National Institutes of Health (grant no. 1DP2OD007307-01).

Author contributions

G.Z. initiated this line of investigation, designed and implemented the project. G.Z., R.H. and C.Y. contributed, developed, refined the concept and wrote the paper.

Additional information

Supplementary information is available in the online version of the paper. Reprints and permissions information is available online at www.nature.com/reprints. Correspondence and requests for materials should be addressed to G.Z.

Competing financial interests

G.Z. and C.Y. are named inventors on a number of related patent applications. G.Z. and C.Y. also have a competing financial interest in Clearbridge Biophotonics and ePetri, Inc., which, however, did not support this work.

Supporting materials

Guoan Zheng*, Roarke Horstmeyer, and Changhuei Yang

Electrical Engineering, California Institute of Technology, Pasadena, CA 91125, USA

*Correspondence should be addressed to: gazheng@caltech.edu

Supplementary Note 1: Computational cost of FPM

Assuming each captured low-resolution intensity image contains n raw pixels and we use m different LEDs for illumination, the computational complexity of the FPM algorithm can be estimated through the following steps: 1) In step 2 of the recovery process, we perform a fast Fourier transform (FFT) to generate the low-resolution image $\sqrt{I_l}e^{i\varphi_l}$. The corresponding computational cost is $n \cdot \log(n)$. 2) In step 3, we perform another FFT to update the corresponding region of the Fourier space of $\sqrt{I_{hr}}e^{i\varphi_{hr}}$. The corresponding computational cost is $n \cdot \log(n)$. 3) In step 4, the above computation is repeated for all incident angles. Thus, the total cost becomes $m \cdot 2 \cdot n \cdot \log(n)$. 4) In step 5, the entire computation is repeated r times, leading to a final computational complexity of $2 \cdot r \cdot m \cdot n \cdot \log(n)$. In our experiment, we use $r = 2$, leading to a computational complexity of $4 \cdot m \cdot n \cdot \log(n)$. Other steps during the recovery process add a negligible amount of computation time compared to the above four operations.

Supplementary Note 2: Simulations of FPM

A simple simulation clearly illustrates the principle of FPM, as shown in Fig. S1. We use a simulated object with the intensity and phase profiles in Fig. S1(a1) and S1(a2), respectively. The pixel size for the two displayed input profiles is 275 nm and the wavelength of the simulated incident illumination is 632 nm. The simulated thin object is illuminated with plane waves from 137 different incident angles, filtered by a 2X objective lens (0.08 NA) and then the field's intensity is recorded by an image sensor with 5.5 μ m pixel size, which is the same as the pixel size at the image plane in our experimental setup. In this first set of simulations, we assume the sample is placed at the focal plane of the objective lens. The resulting low-resolution intensity images, with one percent random speckle noise added to each, are shown in Fig. S1(b) (9 out of the 137 total images are displayed). These low-resolution images then lead to a final reconstructed high-resolution image following the FPM's iterative recovery procedure. A maximum synthetic NA of 0.5 is achieved. Reconstructed intensity, phase, and the Fourier power spectrum are shown in Fig. S1(c). Highlighted regions in Fig. S1(c3) correspond to intensity measurements shown in Fig. S1(b).

Second, we performed a set of simulations to validate FPM's digital wavefront correction procedure in Fig. S4. The leftmost column of Fig. S4 shows 4 simulated images of an object at different locations along the axis of propagation (i.e., the z-direction). Each image exhibits a different amount of defocus aberration. Columns 2 and 3 are the recovered high-resolution intensity and phase profiles achieved using FPM's digital wavefront correction technique. Column 4 and 5 are the recovered high-resolution intensity and phase profiles without using the digital wavefront correction technique. From this comparison, we can see that the second order

defocus aberration can be compensated for up to significantly large defocus distances via wavefront correction.

Supplementary Note 3: Sampling requirement of FPM

The FPM procedure iteratively stitches together a number of low-resolution microscopy images in Fourier space to generate an accurate high-resolution image reconstruction. In the Fourier domain, we work with the complex electric field E associated with the object (its amplitude and phase are recovered during iteration, similar to phase retrieval methods). The final high-resolution reconstruction, on the other hand, is for the object intensity I ($I = E \cdot E^*$, where * denotes complex conjugation). Multiplication of the electric field in the spatial domain corresponds to a convolution operation in the Fourier domain. As such, the passband of the reconstructed intensity image doubles in width in the Fourier domain. Thus, the Nyquist limit for the reconstructed intensity image pixel size becomes $\lambda/(4 \cdot NA_{\text{syn}})$ at the object plane.

Under red illumination (632 nm), this Nyquist pixel size limit is 0.37 μm . The demonstrated SBP of our FPM prototype is therefore 0.9 billion (120 mm^2 FOV divided by the $0.37^2 \mu\text{m}^2$ Nyquist pixel area at 632 nm). In our prototype, the pixel size for each raw image is 2.75 μm at the object plane. For simplicity, we choose a reconstructed pixel size of 0.275 μm (an enhancement factor of 10), in accordance with the Nyquist requirement.

Supplementary Note 4: Estimation of pupil functions

We applied the digital wavefront correction strategy described in the text to additionally compensate for spatially varying aberrations of the employed 2X objective lens. In the following, we provide a simple calibration process for pupil function characterization (other aberration measurement techniques can also be used for this purpose). 1) We first spin coat a layer of 10-micron microspheres (Polysciences Inc.) on top of a microscope slide to create a calibration target. 2) We move the microscope stage -400 μm to +400 μm from the focal plane (50 μm per defocus step), acquiring one image of the calibration target under collimated plane wave illumination at each defocus position (17 images in total). 3) We automatically identify approximately 350 microspheres over the entire FOV of 2X objective lens using a simple digital search procedure. We choose one microsphere at the center FOV and recover its complex profile using a conventional multi-plane phase retrieval algorithm with 17 intensity measurement planes (one image for each plane). The recovered complex image of this single microsphere serves as a microsphere's "ground truth" complex field. 4) We then choose a microsphere at an off-axis position (i.e., away from the center FOV) and initialize an estimate of the pupil function at that location. Specifically, we approximate the pupil function with 5 (or more) Zernike modes, corresponding to x-tilt, y-tilt, x-astigmatism, y-astigmatism, defocus (and higher order aberrations) that may influence the point-spread function at the chosen off-axis microsphere location. We use this pupil function estimate to modify the captured 17 "ground truth" images of the central microsphere to generate a new set of aberrated ground truth defocus intensity images. We then adjust the values of the 5 (or more) unknown parameters to minimize the difference between this set of aberrated intensity images and the actual intensity measurements of the off-axis microsphere. The corresponding pupil function described by 5 (or more) Zernike modes is recovered when the mean-squared error difference is minimized. 5) Step 4 is repeated for other microspheres at different locations within the FOV. We determine each Zernike mode for approximately 350 microspheres, corresponding to 350 locations within the image. 6) Finally,

we fit these 350 values into a polynomial function $z(x, y)$, where (x, y) are spatial coordinates across the image and z denotes the amount of specific Zernike aberration at any pixel along (x, y) . This polynomial function can be used to determine a modified phase map $\varphi(k_x, k_y)$.

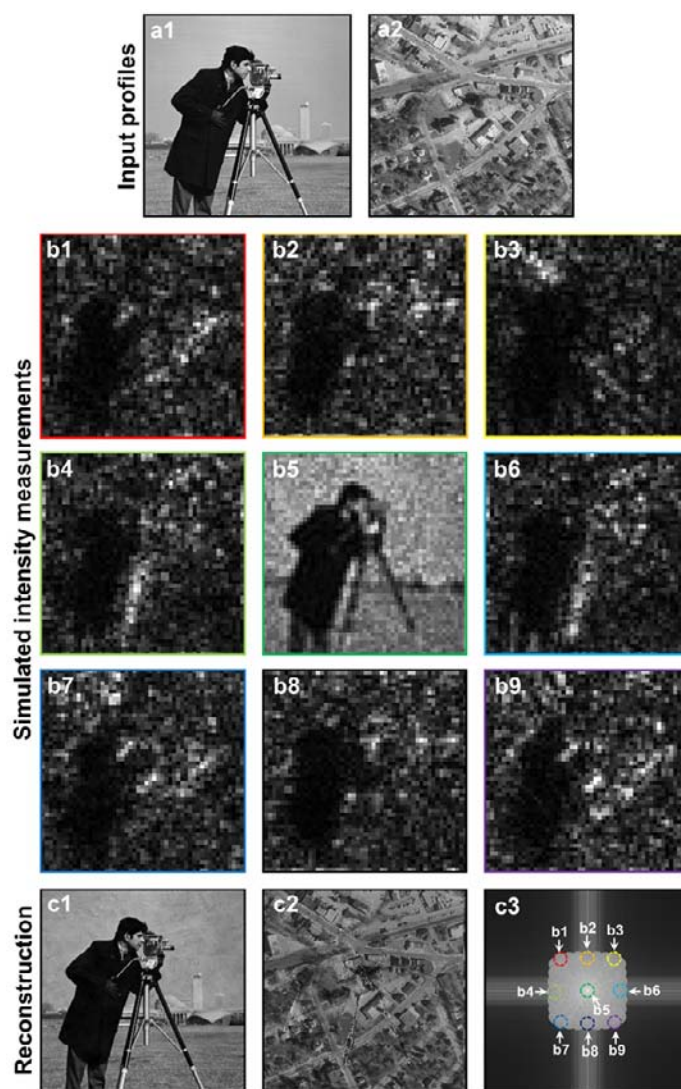


Fig. S1 Simulations of the FPM method. (a1-a2) Input intensity and phase profile of a simulated object, with a pixel size of 275 nm. (b1)-(b9) Simulated low-resolution intensity measurements of the input image (9 out of 137 are displayed), assuming a wavelength of 632 nm, a capturing NA of 0.08, and a 2.75 μm sampling pixel size. (c1-c2) The reconstructed intensity and phase images based on the simulated low-resolution intensity measurements. The pixel size of reconstructed images is 275 nm, the same as the original input. (c3) The Fourier power spectrum of the recovered complex image, displayed on a logarithmic scale. Circled regions correspond to each intensity measurement shown in (b).

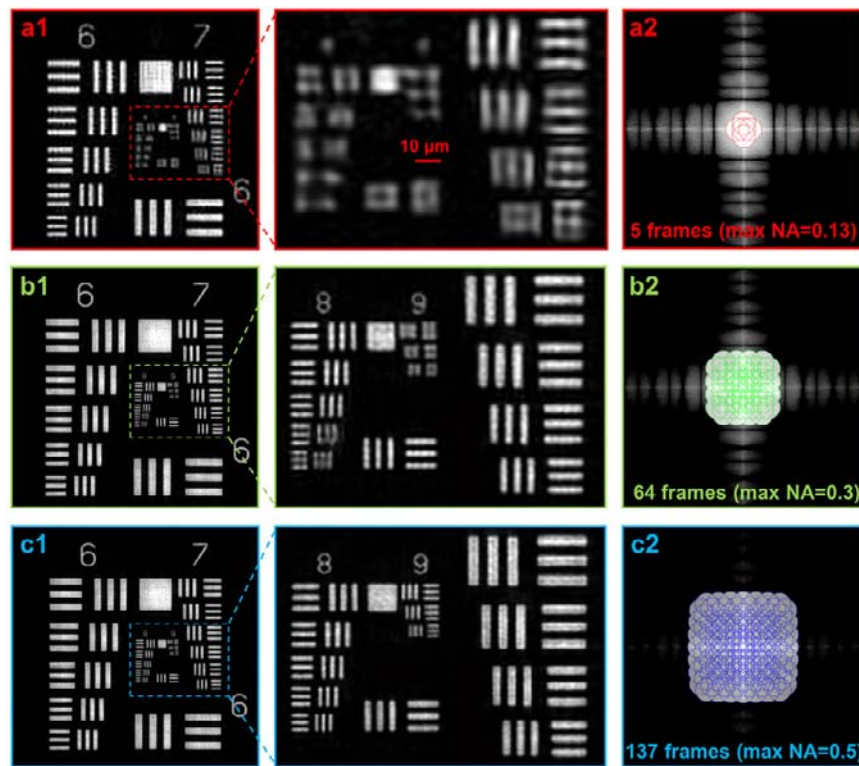


Fig. S2 FPM reconstructions using different numbers of LED light sources with corresponding Fourier power spectrums. (a) A reconstruction using 5 input images, with a maximum NA of 0.13. (b) A reconstruction using 64 input images, with a maximum NA of 0.3. (c) A reconstruction using 137 input images, with a maximum NA of 0.5. Each small circle in (a2)-(c2) represents the spectrum region corresponding to one low-resolution input image.

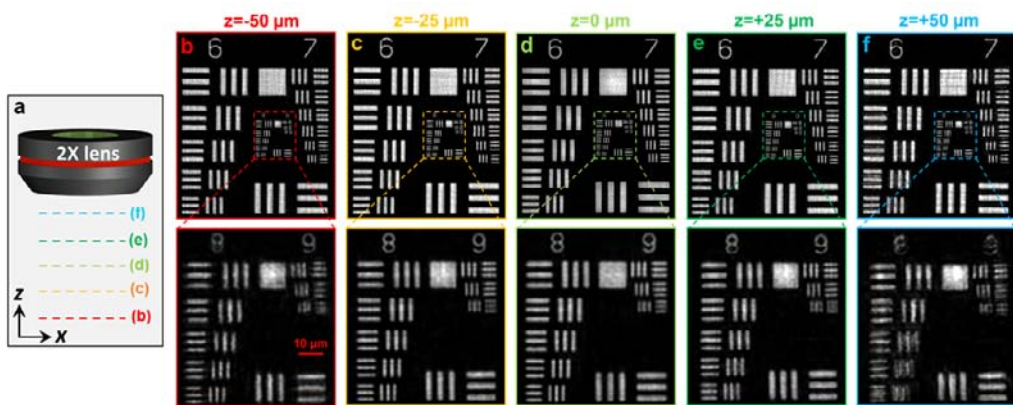


Fig. S3 Depth-of-focus characterization. (a) Experimental scheme: the USAF target is positioned at different locations along the optical axis (i.e., different z-positions), with defocus distances ranging from $-50\text{ }\mu\text{m}$ to $+50\text{ }\mu\text{m}$. (b)-(f) The corresponding FPM reconstructions from each defocus position. These reconstructions do not use our proposed digital wavefront correction procedure.

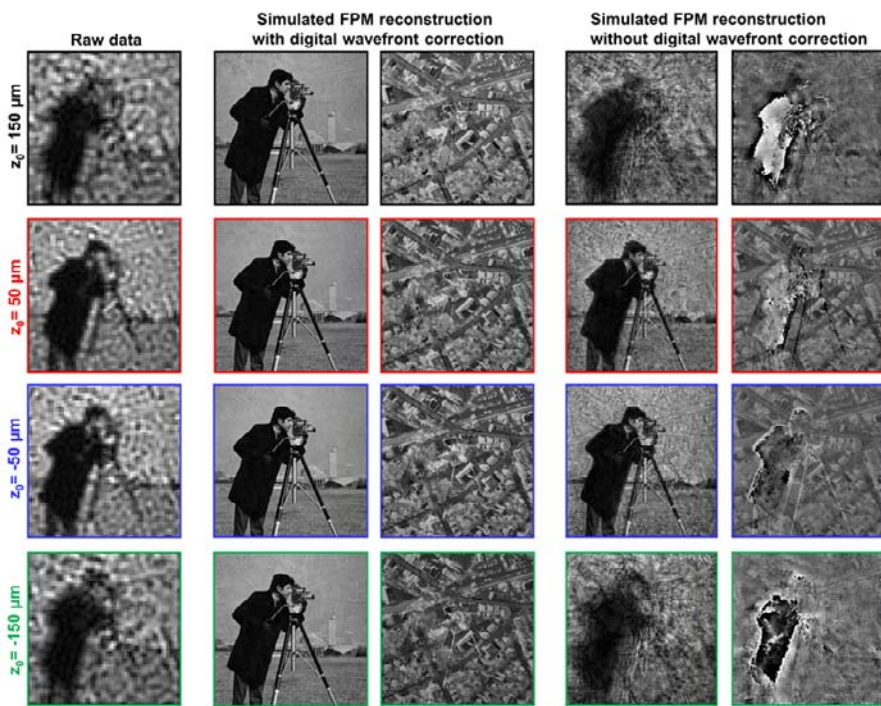


Fig. S4 Correcting aberrations with digital wavefront correction, simulation. Each row contains simulated data assuming an object at different defocus planes, ranging from $-150 \mu\text{m}$ to $+150 \mu\text{m}$ from the focal plane. Here, we use the same simulated object from Fig. S1. Column 1 displays one low-resolution intensity image at each defocus position. Column 2 and 3 are the recovered high-resolution intensity and phase profiles using FPM's digital wavefront correction. Column 4 and 5 are the recovered high-resolution intensity and phase profiles without digital wavefront correction, clearly exhibiting errors.

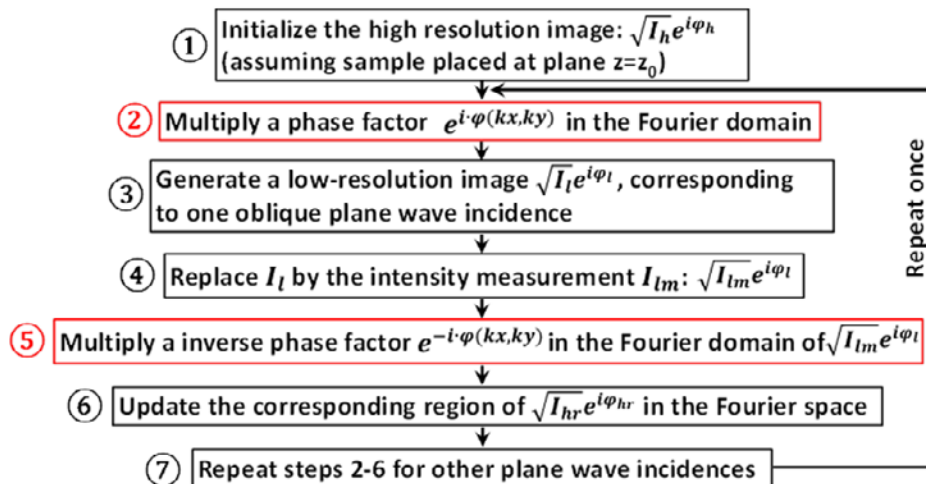


Fig. S5 FPM flowchart with digital wavefront correction. A digital pupil function is introduced in steps 2 and 5 to model the connection between the actual sample profile and the captured intensity data, which may exhibit aberrations caused by defocus.

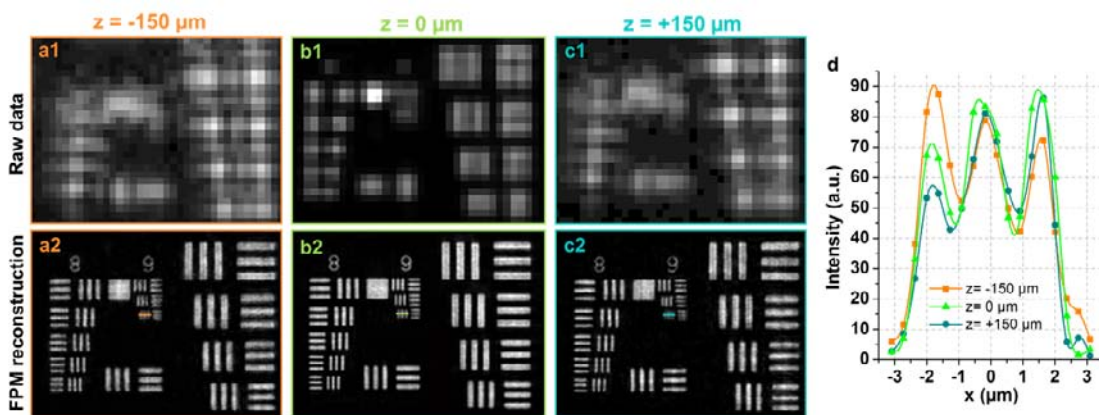


Fig. S6 Correcting aberrations with digital wavefront correction, experiment. (a1)-(c1) Low-resolution raw data of our USAF resolution target, each corresponding to different defocused distances ($-150 \mu\text{m}$ to $150 \mu\text{m}$). (a2)-(c2) FPM's high-resolution image reconstructions using digital wavefront correction. (d) Line traces for the smallest features in (a2)-(c2), with a minimum contrast difference of $\sim 30\%$.

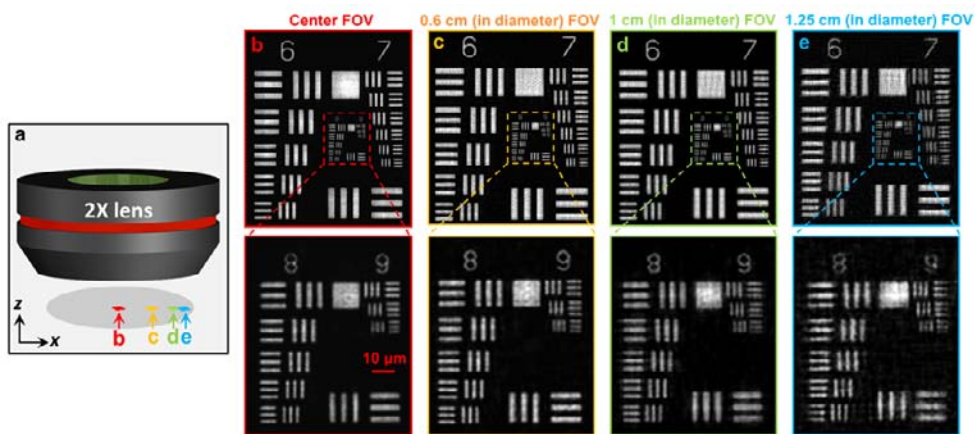


Fig. S7 Resolution enhancement across the entire image field-of-view. (a) Experiential scheme: the USAF resolution target is moved to different positions from the center to the edge of the FOV. (b)-(e) The corresponding FPM reconstructions at 0, 0.6, 1 and 1.25 cm away from the FOV center, respectively. This experiment establishes that the effective FOV of the FPM prototype is $\sim 120 \text{ mm}^2$.

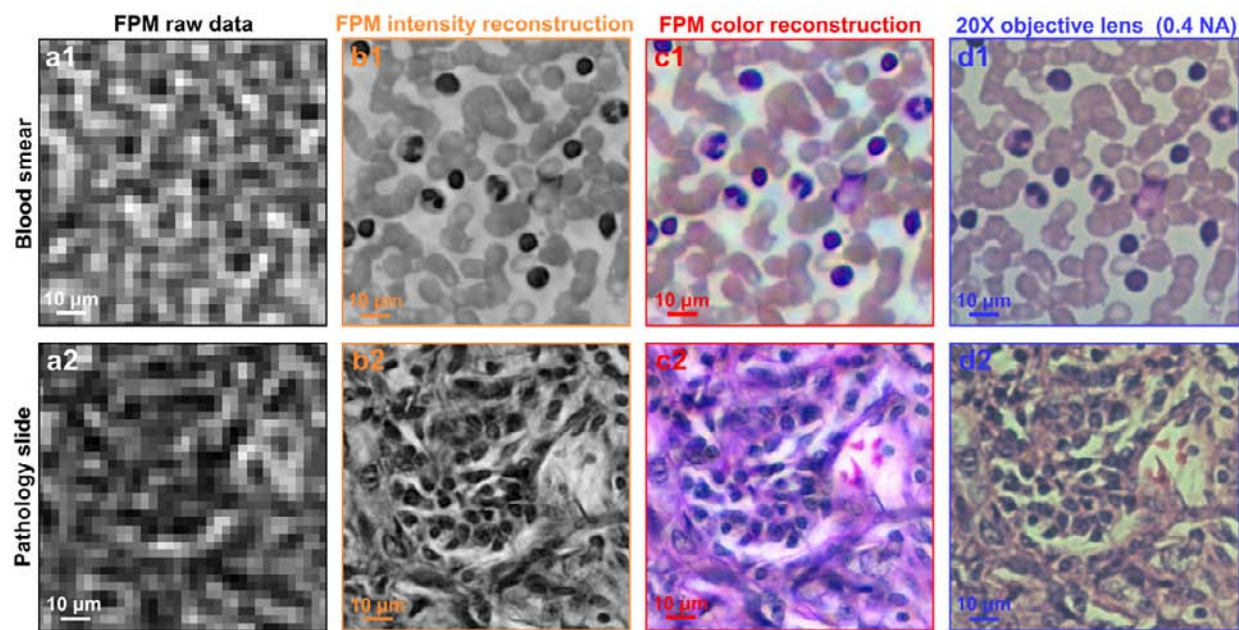


Fig. S8 High-resolution intensity and color imaging via FPM. (a) One low-resolution raw intensity image of a blood smear (a1) and a pathology slide (a2). (b) The corresponding FPM high-resolution intensity image reconstructions. (c) The same reconstructions achieved in color, using three colored wavelengths for illumination. (d) Conventional microscope images under a 20X objective lens.

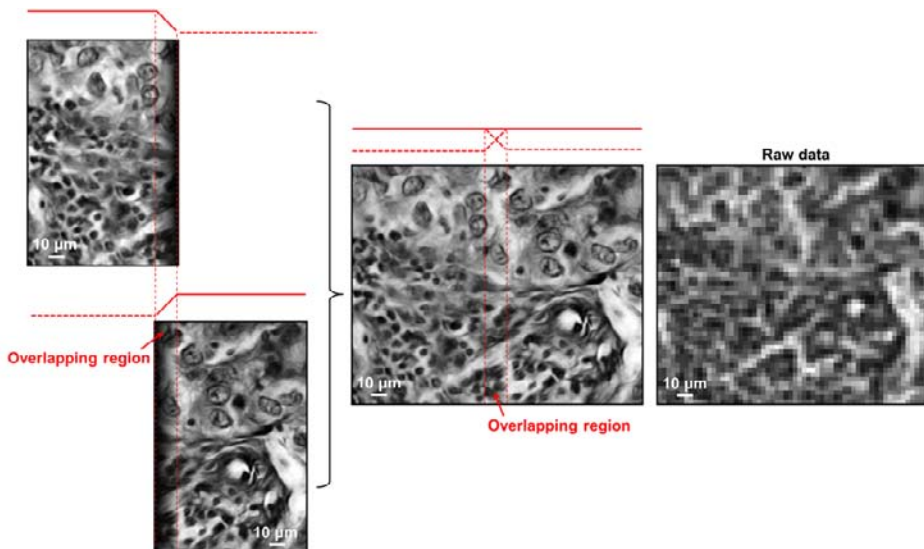


Fig. S9 Demonstration of image segment recombination. As part of our proposed parallelization of data processing, the large format raw image (5280 by 4380) is divided into smaller portions (150 by 150 raw pixels) for computation. For the reconstructed image (1500 by 1500 pixels), we cut away 50 pixels at the edge and use another 50 pixels to overlap with the adjacent portions, introducing a small degree of redundancy into our processing. Images to the left are two adjacent recovered high-resolution image segments, where their overlapping region is denoted. Images to the right demonstrate how image segments are combined using alpha blending to remove any edge artifacts. No observable boundary is present in the stitched region. This blending comes at a small computational cost of redundantly processing the regions of overlap twice.